Bull Eng Geol Environ
DOI 10.1007/s10064-014-0683-8

ORIGINAL PAPER

Borehole seismic surveys for the mechanical characterization of a calcarenite cliff in the area of Ispica (southern Sicily)

S. Imposa · G. Mele · M. Corrao · G. Coco

Received: 15 January 2014 / Accepted: 23 September 2014

Abstract In this study, we investigate the mechanical properties of the substrate underlying the historical Franciscan Friars Minor convent of Ispica (southern Sicily). The convent, where new fractures recently occurred, is located on top of a calcarenite cliff formed along one of the planes of the regional Pozzallo-Ispica-Rosolini normal fault system. Taking advantage of three existing mechanical drillings 30 m deep, we have carried out downhole tests and a seismic tomography survey in uphole configuration. The downhole tests provided vertical profiles of P-wave and S-wave velocities measured at 1 m depth intervals, from which we have derived the basic elastodynamic and seismic parameters, while the tomography survey imaged vertical sections of P-wave velocity across the cliff. The results highlight variable mechanical properties of the subsoil and a step-like pattern of velocity variations parallel to the cliff face that could suggest the occurrence of secondary ruptures related to the main Ispica fault.

Keywords Downhole tests · Uphole seismic tomography · Ispica · Sicily

S. Imposa
Dipartimento di Scienze Biologiche, Geologiche e Ambientali, Sezione di Scienze della Terra, Università degli Studi di Catania, Corso Italia 57, 95129 Catania, Italy

G. Mele (✉)
Istituto Nazionale di Geofisica e Vulcanologia, Via di Vigna Murata 605, 00143 Rome, Italy
e-mail: giuliana.mele@ingv.it

M. Corrao · G. Coco
Geocheck S.r.l., Via Stazzone 45, 95025 Aci Sant'Antonio, CT, Italy

Introduction

This study was undertaken to determine the stiffness of the subsoil beneath and around a historical building where recent fractures occurred. The building stands next to a subvertical fault escarpment where a previous study has pointed out potential stability problems due to the intense fracturing and to the presence of unstable boulders (Imposa et al. 2010).

Seismic surveys are commonly used for engineering geology purposes. The propagation of naturally or artificially produced seismic waves through a geologic medium is used to map 1-D to 3-D distributions of velocity that are indicative of its physical properties (e.g., Bishop et al. 1985; Hunter et al. 2002; Price 2009), and to detect seismic impedance contrasts that occur at lithological or structural/reologic boundaries. These are relevant to seismic ground response (e.g., Cultrera et al. 2003; Bonnefoy-Claudet et al. 2009). As for any geophysical method, seismic surveys yield indirect information that should be integrated and correlated with real geologic data.

Continuous efforts to improve data processing and equipments (e.g., McMechan 1983; Pullan and MacAulay 1987; Bregman et al. 1989; Park et al. 2008) have recently favored a wider use of borehole seismic techniques, developed in the 1950s mainly for reservoirs exploration (e.g., Bois et al. 1972 and references therein); borehole surveys are well suited for the mechanical characterization of the geologic materials and to resolve underground features such as cavities, fracture zones, and velocity reversals (e.g,. Liu et al. 1991; Cosma et al. 2001; Louis and Makropoulos 2001). Measurements with different configurations, well-to-well or well-to-surface and vice versa, depend on the number of drillings and the distance between the holes.

Published online: 21 October 2014

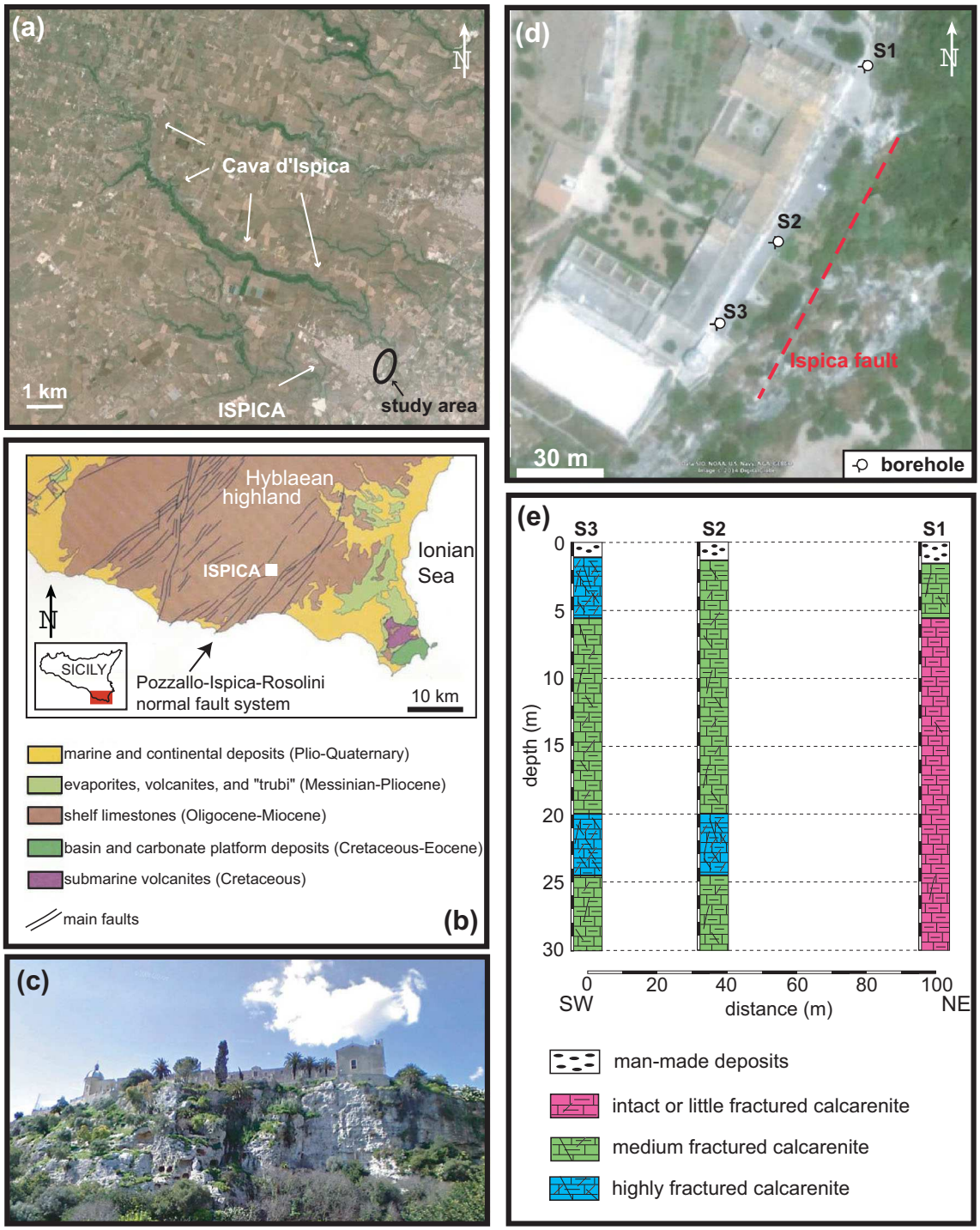

Fig. 1 **a** Google Earth image centered on the Cava d'Ispica fluvial incision, showing the village of Ispica and the study area. **b** Geologic map of southeastern Sicily (after Lentini 1986). **c** Photograph of the Franciscan Friars Minor convent of Ispica and the cliff under investigation (view from the SE). **d** Google Earth image of the convent; the location of the mechanical drillings S1–S3 and the trace of the Ispica fault are indicated. **e** Stratigraphic logs of S1–S3 redrawn after Imposa et al. (2010)

With respect to conventional surface investigations, the main advantage of the borehole surveys is that sources or receivers are placed in the drill hole and the wave paths are one-way; shorter propagation paths imply that signal attenuation is lower and that the sampled volume is smaller, which ensure higher resolution measurements. On the other hand, since mechanical drillings are invasive and cost-effective the use of borehole techniques is limited for

research purposes and, consequently, in the scientific literature, while it is more common in privately commissioned surveys, illustrative applications of these techniques can be also found on commercial websites.

As for this study, the presence of three drill holes previously excavated to 30 m in depth offered us the twofold opportunity to apply borehole techniques with no additional cost for the drilling and to correlate the results with the available stratigraphic logs. The contribution of our work was to complement the geotechnical and kinematic analysis of Imposa et al. (2010) with measurements of the dynamic properties of the subsoil and a more extended mapping of the fractured zone.

In the following sections, we describe the geology of the site, the data acquisition and analysis, and a tentative interpretation of the results compared with direct geologic evidence.

Site description

The survey was carried out in the historical village of Ispica, located at the southeastern end of a 12 km fluvial incision (Cava d'Ispica) within the calcareous Hyblaean highland (Fig. 1a, b). The highland is composed of shelf limestones of the Oligo-Miocene age crossed by mostly extensional faults (Fig. 1b); one of the largest is the Pozzallo-Ispica-Rosolini fault system that extends NE–SW for about 20 km across the study area (e.g., Lentini, 1986; Grasso et al. 1992; Catalano et al. 2004).

The object of this study is a cliff where, at an elevation of ~120 m a.s.l. stands the Franciscan Friars Minor convent built in 1515 (Fig. 1c). Three mechanical drillings (S1–S3) have been excavated in front of the building façade and at short distance from the cliff subvertical escarpment formed along the Ispica fault (Fig. 1d). The boreholes are drilled in 1–2 m of man-made ground and the Miocene calcarenite of the Ragusa Formation (Fig. 1e) (Imposa et al. 2010). This last shows a variable degree of fracturing from place to place and along depth with S1 drilled in ~25 m of intact to little-fractured calcarenite and few metres of medium-fractured rock, while S2 and S3 are mostly drilled in highly fractured rock.

Downhole tests (DHT)

In the downhole tests, travel times of compressional (P) and shear (S) waves generated by a surface source are recorded at regular depth intervals to derive 1-D profiles of velocity from which the main elastodynamic and seismic parameters can be computed. Unlike traditional refraction methods, these tests are able to detect velocity inversions since the travel times are measured as far as the waves penetrate into the medium (direct waves).

Seismic velocity

In this work, P-waves and S-waves are produced by striking vertically and horizontally, with a hammer of 8 kg, a metal plate of 30 cm of diameter placed 2 m away from the hole axis (Fig. 2a). Such a distance makes acceptable the assumption that we are recording nonrefracted arrivals.

We used the pseudo-interval method, i.e., a single receiver is moved inside the borehole (Lai et al. 2000); seismic data are collected at 1 m depth intervals by a triaxial 10 Hz receiver Geospace MP-25, secured to the borehole wall and connected to a 24-bit, 24-channel seismograph MAE A6000S with a bandwidth of 2 Hz–30 kHz.

The vertical travel time tv of P-waves (first pulse) and S-waves is computed as:

$$\mathrm{tv} = t\cos\alpha, \tag{1}$$

where t is the one-way travel time and α is the angle between the borehole axis and the line connecting the geophone and the source (Fig. 2a). The S-wave arrival is identified by rotating the two horizontal components of the ground motion until the S-waves have opposite peaks and the largest amplitude at the same time.

The interval velocity (V_i) is computed dividing the distance between two adjacent positions of the geophone h_i and h_{i-1} by the vertical travel times difference:

$$V_i = \frac{h_i - h_{i-1}}{\mathrm{tv}_i - \mathrm{tv}_{i-1}}. \tag{2}$$

Figure 2b shows the vertical profiles of Vp and Vs compared with the borehole logs. We have carried out the DHT below the man-made deposits, from 2 to 30 m of depth at S1 and S2 and from 1 to 29 m of depth at S3. The larger velocity measured at S1 (Vs and Vp mostly higher than 1,000 and 2,500 m/s, respectively) with respect to S2 and S3 (Vs and Vp mostly lower than 1,000 and 2,500 m/s, respectively) is consistent with the less fractured rock drilled at this site.

Elastodynamic and seismic parameters

We used the Vp and Vs values determined from the DHT and the rock density (ρ) measured in the samples collected from the boreholes to calculate the following elastodynamic parameters (1–5) and seismic parameters (6–7) at 1 m intervals:

1. Rigidity (or shear) modulus, measuring the response of a medium to shear strain:

$$G_{\mathrm{din}} = \rho V_S^2; \tag{3}$$

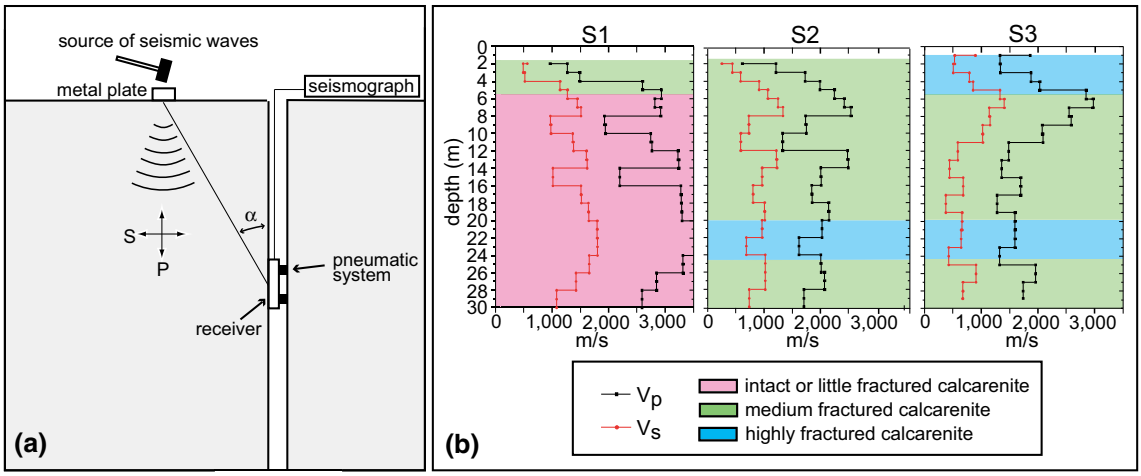

Fig. 2 **a** Sketch illustrating the configuration used for the downhole tests. The receiver is secured to the borehole wall through a pneumatic system. **b** Vertical profiles of P-wave and S-wave velocity measured at 1 m intervals inside the holes S1–S3; the background colors of the diagrams are indicative of the degree of fracturing resulting from the borehole logs. The DHT are carried out below the man-made deposits

2. Bulk (or compressibility) modulus, measuring the relative volume change of a medium when a pressure change is applied:

$$K_{\mathrm{din}} = \rho\left(V_{\mathrm{P}}^2 - \frac{4}{3}V_{\mathrm{S}}^2\right); \tag{4}$$

3. Elasticity (or Young's) modulus, describing the tendency of a medium to deform along an axis when opposing forces are applied along that axis:

$$E_{\mathrm{din}} = gV_{\mathrm{S}}^2\frac{(3V_{\mathrm{P}}^2 - 4V_{\mathrm{S}}^2)}{(V_{\mathrm{P}}^2 - V_{\mathrm{S}}^2)}, \tag{5}$$

where g is the acceleration of gravity;

4. Geophysical (or bulk) density, indicating the status of aggregation of the medium. It is computed from the following empirical relationship (Gardner et al. 1974):

$$\gamma_{\mathrm{din}} = aV_{\mathrm{P}}^m, \tag{6}$$

where the parameters a and m are defined for various lithologies (e.g., Quijada and Stewart 2007). In this work, $a = 0.51$ and $m = 0.19$ gave results that agree quite well with the laboratory measurements;

5. Poisson's ratio, measuring the degree of transverse deformation of a material strained longitudinally:

$$\sigma = \frac{V_{\mathrm{P}}^2 - 2V_{\mathrm{S}}^2}{2(V_{\mathrm{P}}^2 - V_{\mathrm{S}}^2)}; \tag{7}$$

6. S-wave seismic impedance, affecting the reflectivity of seismic energy in a medium and, therefore, the local amplification of ground motion:

$$Z_{\mathrm{S}} = \rho V_{\mathrm{S}}; \tag{8}$$

7. Reflection (R) and transmission (T) coefficients, describing how much of a seismic wave is reflected and transmitted by an impedance discontinuity occurring in a medium; for a plane P wave normally incident on a flat discontinuity, they are defined as:

$$R = \frac{Z_{\mathrm{P2}} - Z_{\mathrm{P1}}}{Z_{\mathrm{P2}} + Z_{\mathrm{P1}}}; \tag{9}$$

$$T = \frac{2Z_{\mathrm{P2}}}{(Z_{\mathrm{P2}} + Z_{\mathrm{P1}})^2}, \tag{10}$$

where Z_{P1} and Z_{P2} are the seismic impedance in the two layers separated by the discontinuity.

The depth variation of the elastodynamic and seismic parameters, listed in Tables 1, 2, 3, show that the quality of the substrate decreases from NE (drilling S1) to SW (drilling S3) (Fig. 3).

In addition, we have computed the average shear wave velocity in the topmost 30 m that is used for the seismic characterization of the foundation soil (e.g., Kanli et al. 2006; Roser and Gosar 2010; Bala et al. 2013):

$$Vs_{30} = \frac{30}{\sum_{i=1,30}\frac{h_{\mathrm{i}}}{Vs_{\mathrm{i}}}}, \tag{11}$$

where h_{i} and Vs_i indicate thickness and shear wave velocity (for shear strains $<10^{-6}$) in the ith interval. The Vs_{30} parameter is used by several national seismic regulations to classify the ground in five major types (A–E) and two categories specific for soft and liquefiable soil (S1–S2), according to the building Eurocode 8 standard (CEN 2004).

Table 1 Elastodynamic and seismic parameters computed at S1

h (m)	Seismic velocity			Elastodynamic moduli					Seismic parameters		
	V_P (m/s)	V_S (m/s)	V_P/V_S	σ	γ (g/cm^3)	G (kg/cm^2)	K (kg/cm^2)	E (kg/cm^2)	Zs (g/(m^{2}s))	T	R
2	968.64	565.69	1.71	0.2412	1.88	6.1E+03	9.8E+03	1.5E+ 04	1,065.41	0.9974	0.0026
3	1,267.14	492.40	2.57	0.4111	1.98	4.9E+03	2.6E+04	1.4E+ 04	975.94	1.4536	−0.4536
4	1,492.29	518.43	2.88	0.4314	2.04	5.6E+03	3.9E+04	1.6E+ 04	1,059.98	1.4730	−0.4730
5	2,598.46	1,142.96	2.27	0.3801	2.27	3.0E+04	1.2E+05	8.3E+ 04	2,596.56	1.1247	−0.1247
6	2,930.71	1,274.57	2.30	0.3834	2.32	3.8E+04	1.5E+05	1.1E+ 05	2,962.51	1.0855	−0.0855
7	2,812.16	1,446.74	1.94	0.3200	2.31	4.9E+04	1.2E+05	1.3E+ 05	3,336.39	0.7703	0.2297
8	2,923.75	1,513.69	1.93	0.3169	2.32	5.4E+04	1.3E+05	1.4E+ 05	3,516.70	0.7504	0.2496
9	1,927.08	973.70	1.98	0.3286	2.15	2.1E+04	5.3E+04	5.5E+ 04	2,089.91	1.2009	−0.2009
10	1,942.15	982.53	1.98	0.3280	2.15	2.1E+04	5.4E+04	5.6E+ 04	2,111.97	1.2007	−0.2007
11	2,744.10	1,368.34	2.01	0.3345	2.30	4.3E+04	1.2E+05	1.2E+ 05	3,140.95	1.0964	−0.0964
12	2,766.12	1,380.17	2.00	0.3343	2.30	4.4E+04	1.2E+05	1.2E+ 05	3,172.91	1.0950	−0.0950
13	3,226.22	1,610.03	2.00	0.3342	2.37	6.2E+04	1.7E+05	1.7E+05	3,811.14	0.7385	0.2615
14	3,244.78	1,619.90	2.00	0.3340	2.37	6.3E+04	1.7E+05	1.7E+05	3,838.70	0.7360	0.2640
15	2,195.33	1,014.06	2.16	0.3644	2.20	2.3E+04	7.7E+04	6.2E+04	2,231.10	1.2339	−0.2339
16	2,198.93	1,015.57	2.17	0.3644	2.20	2.3E+04	7.7E+04	6.3E+04	2,235.13	1.2343	−0.2343
17	3,276.66	1,513.57	2.16	0.3644	2.37	5.5E+04	1.8E+05	1.5E+05	3,593.39	1.0417	−0.0417
18	3,284.40	1,516.94	2.17	0.3644	2.38	5.5E+04	1.9E+05	1.5E+05	3,603.01	1.0414	−0.0414
19	3,290.72	1,643.93	2.00	0.3337	2.38	6.5E+04	1.7E+05	1.7E+05	3,906.06	1.0528	−0.0528
20	3,295.94	1,646.75	2.00	0.3337	2.38	6.5E+04	1.7E+05	1.7E+05	3,913.93	1.0526	−0.0526
21	3,595.64	1,796.56	2.00	0.3336	2.42	7.9E+04	2.1E+05	2.1E+05	4,341.19	1.0015	−0.0015
22	3,600.25	1,799.03	2.00	0.3336	2.42	7.9E+04	2.1E+05	2.1E+05	4,348.22	1.0013	−0.0013
23	3,604.16	1,801.12	2.00	0.3336	2.42	7.9E+04	2.1E+05	2.1E+05	4,354.17	0.9499	0.0501
24	3,607.49	1,802.90	2.00	0.3335	2.42	8.0E+04	2.1E+05	2.1E+05	4,359.25	0.9497	0.0503
25	3,312.34	1,655.54	2.00	0.3335	2.38	6.6E+04	1.8E+05	1.8E+05	3,938.54	0.9099	0.0901
26	3,314.29	1,656.59	2.00	0.3335	2.38	6.6E+04	1.8E+05	1.8E+05	3,941.47	0.9098	0.0902
27	2,845.50	1,422.38	2.00	0.3334	2.31	4.7E+04	1.3E+05	1.3E+05	3,287.58	0.8538	0.1462
28	2,846.44	1,422.89	2.00	0.3334	2.31	4.7E+04	1.3E+05	1.3E+05	3,288.97	0.8537	0.1463
29	2,589.80	1,078.70	2.40	0.3950	2.27	2.7E+04	1.2E+05	7.5E+04	2,449.02	0.0000	1.0000
30	2,590.34	1,078.85	2.40	0.3951	2.27	2.7E+04	1.2E+05	7.5E+04	2,449.46	0.0000	1.0000

Based on this parameter, the subsoil at S1 (Vs_{30} = 1,134.58 m/s) is classified as type A ($Vs_{30} > 800$ m/s: rock or other rock-like geological formation, including at most 5 m of weaker material at the surface), while the subsoil at S2 and S3 (Vs_{30} = 724.49 and 646.93 m/s, respectively) is classified as type B (Vs_{30} = 360–800 m/s: deposits of very dense sand, gravel, or very stiff clay, at least several tens of meters in thickness, characterized by a gradual increase of mechanical properties with depth).

Uphole seismic tomography

Seismic tomography is a technique that uses arrays of receivers to record wave travel times, more often the first compressional arrival, in order to construct 2-D or 3-D images of velocity with different methods (e.g., Philips and Fehler 1991; Taillandier et al. 2009); in uphole configuration, seismic waves travel in the rock volume between the borehole and the ground surface (e.g., Lai et al. 2000).

In this work, we have acquired three profiles of different length: TOMO1 (10 m), TOMO2 (100 m), and TOMO3 (24 m), each crossing one of the boreholes equipped with sources or receivers (Fig. 4a). The choice of placing sources or receivers inside a borehole was based on logistics and on the lateral extent of the profile with respect to the borehole location. We have used borehole sources (seismic gun) along TOMO2 to obtain a symmetric distribution of ray paths as this profile extends on both sides of the drilling, and surface sources (hammer) along TOMO1 and TOMO3 that extend only on one side of the borehole. Vertical geophones Geospace GS-11D with a natural frequency of 14 Hz were deployed every 2 m along TOMO1 and TOMO3, and every 5 m along TOMO2. To extend the

Table 2 Elastodynamic and seismic parameters computed at S2

h (m)	Seismic velocity			Elastodynamic moduli					Seismic parameters		
	V_P (m/s)	V_S (m/s)	V_P/V_S	σ	γ (g/cm^3)	G (kg/cm^2)	K (kg/cm^2)	E (kg/cm^2)	Zs (g/(m^{2}s))	T	R
2	617.56	251.42	2.46	0.401	1.73	1.1E+03	5.2E+03	3.1E+03	434.70	1.48	−0.48
3	1,210.63	438.10	2.76	0.425	1.96	3.8E+03	2.4E+04	1.1E+04	860.82	1.39	−0.39
4	1,731.57	584.72	2.96	0.436	2.10	7.3E+03	5.4E+04	2.1E+04	1,229.77	1.32	−0.32
5	1,993.29	915.95	2.18	0.366	2.16	1.8E+04	6.2E+04	5.0E+04	1,978.60	1.17	−0.17
6	2,252.33	1,070.00	2.10	0.354	2.21	2.6E+04	7.9E+04	6.9E+04	2,365.67	1.12	−0.12
7	2,426.21	1,250.45	1.94	0.319	2.24	3.5E+04	8.6E+04	9.4E+04	2,803.97	0.71	0.29
8	2,542.40	1,336.07	1.90	0.309	2.26	4.1E+04	9.4E+04	1.1E+05	3,022.70	0.68	0.32
9	1,733.89	727.00	2.39	0.393	2.10	1.1E+04	4.9E+04	3.1E+04	1,529.39	0.87	0.13
10	1,752.27	734.96	2.38	0.393	2.11	1.2E+04	5.0E+04	3.2E+04	1,549.24	0.87	0.13
11	1,327.39	588.45	2.26	0.378	2.00	7.0E+03	2.6E+04	1.9E+04	1,176.65	1.40	−0.40
12	1,331.19	590.48	2.25	0.378	2.00	7.1E+03	2.6E+04	1.9E+04	1,181.35	1.40	−0.40
13	2,477.69	1,220.58	2.03	0.340	2.25	3.4E+04	9.5E+04	9.1E+04	2,747.92	0.86	0.14
14	2,492.75	1,230.04	2.03	0.339	2.25	3.5E+04	9.6E+04	9.2E+04	2,772.42	0.86	0.14
15	2,006.33	965.10	2.08	0.349	2.16	2.0E+04	6.1E+04	5.5E+04	2,087.36	0.90	0.10
16	2,011.35	968.13	2.08	0.349	2.16	2.1E+04	6.1E+04	5.5E+04	2,094.91	0.90	0.10
17	1,848.86	807.16	2.29	0.382	2.13	1.4E+04	5.5E+04	3.9E+04	1,718.87	1.13	−0.13
18	1,851.40	808.32	2.29	0.382	2.13	1.4E+04	5.5E+04	3.9E+04	1,721.78	1.13	−0.13
19	2,150.85	1,013.12	2.12	0.357	2.19	2.3E+04	7.2E+04	6.2E+04	2,220.38	0.97	0.03
20	2,153.58	1,014.64	2.12	0.357	2.19	2.3E+04	7.2E+04	6.2E+04	2,224.25	0.97	0.03
21	2,025.46	967.02	2.09	0.352	2.17	2.1E+04	6.3E+04	5.5E+04	2,095.29	0.81	0.19
22	2,027.08	967.95	2.09	0.352	2.17	2.1E+04	6.3E+04	5.6E+04	2,097.63	0.81	0.19
23	1,619.39	686.97	2.36	0.390	2.08	9.9E+03	4.2E+04	2.8E+04	1,426.55	1.21	−0.21
24	1,619.94	687.19	2.36	0.390	2.08	9.9E+03	4.2E+04	2.8E+04	1,427.09	1.21	−0.21
25	2,010.04	1,019.06	1.97	0.327	2.16	2.3E+04	5.8E+04	6.0E+04	2,204.84	1.00	0.00
26	2,010.94	1,019.67	1.97	0.327	2.16	2.3E+04	5.8E+04	6.0E+04	2,206.36	1.00	0.00
27	2,074.14	1,020.21	2.03	0.340	2.18	2.3E+04	6.4E+04	6.1E+04	2,220.53	0.82	0.18
28	2,074.90	1,020.67	2.03	0.340	2.18	2.3E+04	6.4E+04	6.2E+04	2,221.71	0.82	0.18
29	1,704.90	738.85	2.31	0.384	2.10	1.2E+04	4.6E+04	3.2E+04	1,549.34	0.00	1.00
30	1,705.21	738.97	2.31	0.384	2.10	1.2E+04	4.6E+04	3.2E+04	1,549.66	0.00	1.00

TOMO1 and TOMO2 profiles to the cliff escarpment, receivers and sources were placed down the slope by professional rock climbers (Fig. 4a). The acquisition system is the same used for the DHT.

For the 2-D tomography reconstruction, we used a nonlinear technique known as the generalized simulated-annealing optimization (GSAO) (Pullammanappallil and Louie 1994). Unlike the linear methods, in this algorithm the convergence is independent on the initial model and gives reliable results with little or no a priori constraints. The GSAO algorithm computes synthetic travel times from an initial velocity-depth model represented as discrete cells, each assigned with a constant velocity value; the synthetic travel times are compared to the observed travel times and the least-square error E_0 is determined. The velocity model is perturbed iteratively including random velocity constants and the new E_0 is determined until a "best" model minimizes the discrepancy between calculated and observed travel times.

After 11,000 iterations, we have obtained a final least-square error of 0.002 s^2 for TOMO1, 0.015 s^2 for TOMO2, and 0.005 s^2 for TOMO3; the cells size is $x = 0.291$ m and $y = 0.291$ m for TOMO1, $x = 1.875$ m and $y = 0.937$ m for TOMO2, $x = 0.359$ m; $y = 0.179$ m for TOMO3 (x and y are the horizontal and vertical axes, respectively). Figure 4a–c shows the Vp velocity-depth models and the corresponding ray density diagrams, next to the Vp profile obtained from the downhole tests and the borehole logs.

TOMO1 has the lowest ray coverage that is dense only in the area between the slope of the cliff (shots) and the borehole (receivers); here, the relatively high velocity ($\sim$2,000 m/s) is consistent with the little fractured and

Table 3 Elastodynamic and seismic parameters computed at S3

h (m)	Seismic velocity			Elastodynamic moduli					Seismic parameters		
	V_P (m/s)	V_S (m/s)	V_P/V_S	σ	γ (g/cm^3)	G (kg/cm^2)	K (kg/cm^2)	E (kg/cm^2)	Zs (g/(m^{2}s))	T	R
1	1,863.39	894.43	2.08	2.13	1.7E+04	5.2E+04	4.7E+04	0.350	1,907.54	0.69	0.31
2	1,326.59	529.89	2.50	2.00	5.7E+03	2.8E+04	1.6E+04	0.405	1,059.45	1.23	−0.23
3	1,336.80	503.25	2.66	2.00	5.1E+03	2.9E+04	1.5E+04	0.417	1,007.64	1.30	−0.30
4	1,876.33	788.22	2.38	2.14	1.3E+04	5.8E+04	3.7E+04	0.393	1,683.23	1.29	−0.29
5	2,030.48	857.03	2.37	2.17	1.6E+04	6.9E+04	4.5E+04	0.392	1,857.84	1.28	−0.28
6	2,846.68	1,325.24	2.15	2.31	4.1E+04	1.3E+05	1.1E+05	0.362	3,063.30	0.91	0.09
7	2,987.90	1,405.08	2.13	2.33	4.7E+04	1.5E+05	1.3E+05	0.358	3,277.86	0.89	0.11
8	2,547.35	1,136.25	2.24	2.26	3.0E+04	1.1E+05	8.1E+04	0.376	2,571.58	0.93	0.07
9	2,583.98	1,154.40	2.24	2.27	3.1E+04	1.1E+05	8.4E+04	0.375	2,619.75	0.92	0.08
10	2,077.88	1,020.99	2.04	2.18	2.3E+04	6.5E+04	6.2E+04	0.341	2,223.00	0.70	0.30
11	2,086.69	1,027.06	2.03	2.18	2.3E+04	6.5E+04	6.2E+04	0.340	2,238.01	0.70	0.30
12	1,481.55	585.08	2.53	2.04	7.1E+03	3.6E+04	2.0E+04	0.408	1,194.59	0.85	0.15
13	1,482.43	585.17	2.53	2.04	7.1E+03	3.6E+04	2.0E+04	0.408	1,194.91	0.85	0.15
14	1,354.04	439.04	3.08	2.01	3.9E+03	3.2E+04	1.1E+04	0.441	881.22	1.24	−0.24
15	1,354.39	438.85	3.09	2.01	3.9E+03	3.2E+04	1.1E+04	0.441	880.89	1.24	−0.24
16	1,696.95	680.03	2.50	2.10	9.8E+03	4.8E+04	2.8E+04	0.404	1,424.75	0.69	0.31
17	1,698.30	680.56	2.50	2.10	9.8E+03	4.8E+04	2.8E+04	0.404	1,426.06	0.69	0.31
18	1,278.38	375.09	3.41	1.99	2.8E+03	2.9E+04	8.2E+03	0.453	744.68	1.30	−0.30
19	1,278.54	374.99	3.41	1.99	2.8E+03	2.9E+04	8.2E+03	0.453	744.50	1.30	−0.30
20	1,592.84	663.14	2.40	2.07	9.2E+03	4.1E+04	2.6E+04	0.395	1,372.74	0.98	0.02
21	1,593.45	663.47	2.40	2.07	9.2E+03	4.1E+04	2.6E+04	0.395	1,373.53	0.98	0.02
22	1,594.00	642.52	2.48	2.07	8.7E+03	4.2E+04	2.4E+04	0.403	1,330.25	0.77	0.23
23	1,594.48	642.74	2.48	2.07	8.7E+03	4.2E+04	2.4E+04	0.403	1,330.78	0.77	0.23
24	1,321.79	420.61	3.14	2.00	3.6E+03	3.1E+04	1.0E+04	0.444	840.37	1.40	−0.40
25	1,321.93	420.60	3.14	2.00	3.6E+03	3.1E+04	1.0E+04	0.444	840.37	1.40	−0.40
26	1,952.68	903.92	2.16	2.15	1.8E+04	5.9E+04	4.9E+04	0.364	1,945.00	0.84	0.16
27	1,953.35	904.38	2.16	2.15	1.8E+04	5.9E+04	4.9E+04	0.364	1,946.12	0.84	0.16
28	1,734.24	676.00	2.57	2.10	9.7E+03	5.1E+04	2.7E+04	0.410	1,422.17	0.00	1.00
29	1,734.58	676.14	2.57	2.10	9.7E+03	5.1E+04	2.7E+04	0.410	1,422.51	0.00	1.00

intact calcarenite drilled by S1 but is lower than the *V*p values determined with the DHT that mostly exceed 2,500 m/s (Fig. 4b; Table 1).

TOMO2 displays two major zones of high and low velocity separated by subvertical boundaries, one occurring beneath the convent. At the borehole location, the low *V*p imaged in the first ~12 m is consistent with the medium-fractured calcarenite, but is lower than the *V*p measured with the DHT. Below this depth, TOMO2 attains higher velocity that is in agreement with the DHT but is not consistent with the increasing fracturing shown by the borehole log (Fig. 4c). Although the ray coverage is low, the downward transition from low to high velocity occurring at −12 m matches a sudden increase of ~1,100 m/s detected by the DHT (Fig. 4c; Table 2). The step-like pattern of velocity imaged by TOMO2 could be indicative of high-angle secondary ruptures parallel to the trend of the main Ispica fault, the low velocity being associated with the more fractured damage zone.

TOMO3 is rather homogeneous with *V*p values around 1,000 m/s that are consistent with the DHT and with the medium-to-high degree of fracturing shown by the borehole log. The shallow high-velocity anomaly imaged a few meters away from S3 is probably due to the presence of a more compact calcarenitic block that could also explain the higher velocity sampled by the DHT at a depth of 6–9 m (Fig. 4d; Table 3).

Conclusions

The object of this study is the dynamic characterization of the subsoil of a Miocene calcareous cliff, on top of which is the ancient Friars Minor Convent of Ispica. The NE–SW

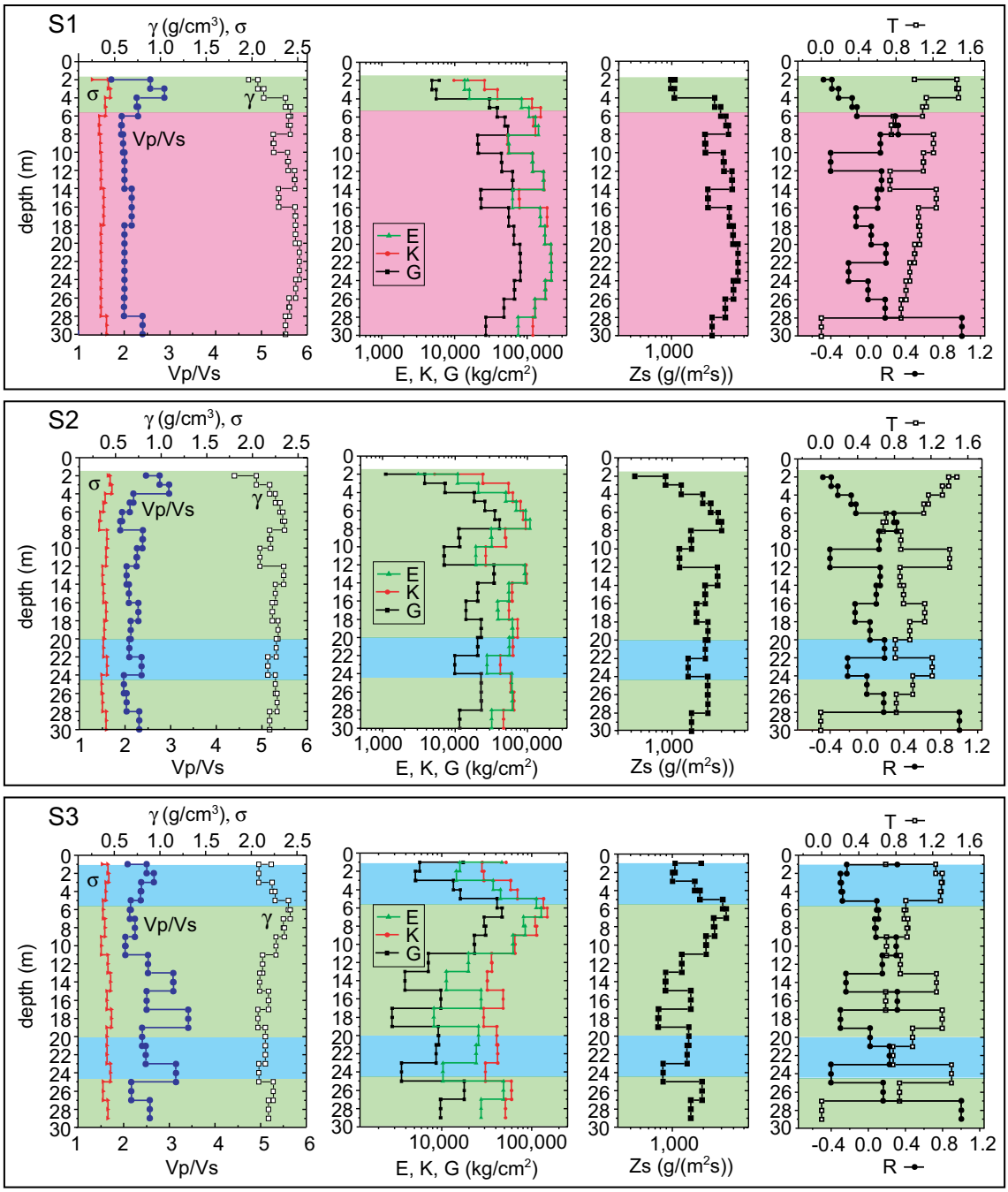

Fig. 3 Depth variations of the elastodynamic and seismic parameters derived at S1–S3 from P-wave and S-wave velocity; the background colors of the diagrams are indicative of the degree of fracturing resulting from the borehole logs (see legend of Fig. 2b)

Ispica fault, belonging to a regional high-angle normal fault system, crosses the study area. The elastodynamic and seismic parameters derived in the present study from the downhole tests highlight that the quality of the subsoil is variable and decreases significantly from north to south. The 2-D velocity distribution imaged from seismic tomography is consistent with this view. One of the tomography profiles shows that the convent front stands on

Fig. 4 **a** (*Left*) Plan of the study area showing the trace of the ▶ tomography profiles, and (*right*) photograph of the installation phase of the seismic array down the cliff escarpment. **b–d** Vertical sections of P-wave velocity and corresponding ray density diagrams; the cells size of the velocity models (*x* horizontal axis; *y* vertical axis) is indicated. Next to the tomograms are shown for comparison the 1-D profiles of *Vp* computed from the downhole tests and the borehole logs. In TOMO2, we tentatively interpret the step-like pattern of velocity as caused by secondary ruptures (*dashed black lines*) parallel to the Ispica fault plane (*dashed red line* in Fig. 4a)

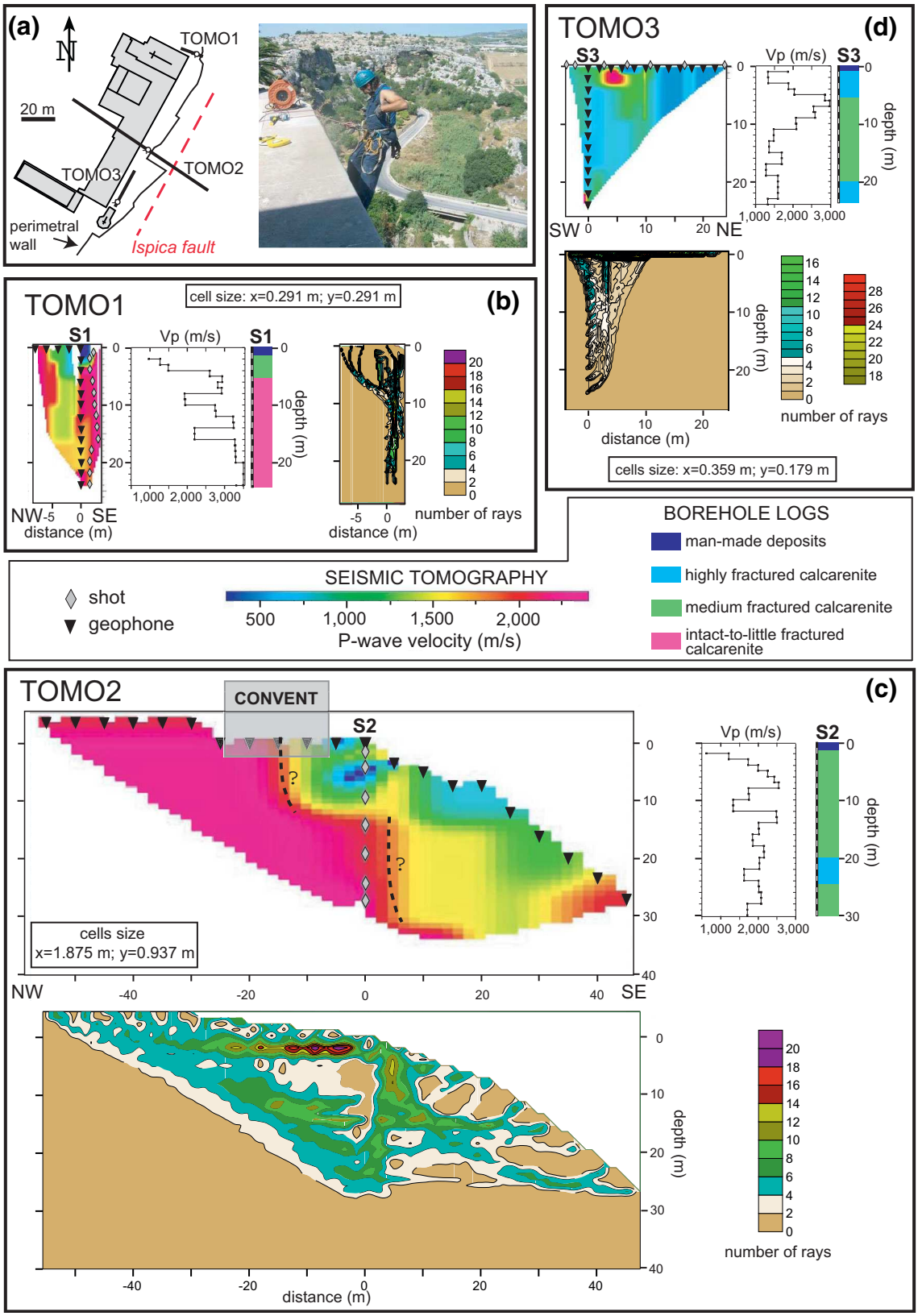
(a)
N
TOMO1
20 m
TOMO3
TOMO2
perimetral wall
Ispica fault
TOMO3
(d)
S3
Vp (m/s)
S3
depth (m)
SW
NE
distance (m)
number of rays
cells size: x=0.359 m; y=0.179 m
TOMO1
cell size: x=0.291 m; y=0.291 m
(b)
S1
Vp (m/s)
S1
depth (m)
NW
SE
distance (m)
number of rays
BOREHOLE LOGS
man-made deposits
highly fractured calcarenite
medium fractured calcarenite
intact-to-little fractured calcarenite
SEISMIC TOMOGRAPHY
shot
geophone
500
1,000
1,500
2,000
P-wave velocity (m/s)
TOMO2
CONVENT
S2
(c)
Vp (m/s)
S2
depth (m)
cells size
x=1.875 m; y=0.937 m
NW
SE
distance (m)
number of rays

a low-quality substrate; the step-like pattern of velocity parallel to the cliff's slope is suggestive of high-angle secondary ruptures related to the main fault escarpment. With respect to the results of Imposa et al. (2010), this study brings new information on the dynamical properties of the subsoil and a more extended mapping of the fracture zones beneath the convent and at depth.

References

Bala A, Arion C, Aldea A (2013) In situ borehole measurements and laboratory measurements as primary tools for the assessment of the seismic site effects. Rom Rep Phys 65(1):285–298

Bishop T, Bube K, Cutler R, Langan R, Love P, Resnick J, Shuey R, Spindler D, Wyld H (1985) Tomographic determination of velocity and depth in laterally varying media. Geophysics 50(6):903–923. doi:10.1190/1.1441970

Bois P, La Porte M, Lavergne M, Thomas G (1972) Well-to-well seismic measurements. Geophysics 37:471–480. doi:10.1190/1.1440273

Bonnefoy-Claudet S, Baize S, Bonilla LF, Berge-Thierry C, Pasten C, Campos J, Volant P, Verdugo R (2009) Site effect evaluation in the basin of Santiago de Chile using ambient noise measurements. Geophys J Int 176:925–937. doi:10.1111/j.1365-246X.2008.04020.x

Bregman ND, Bailey RC, Chapman CH (1989) Crosshole seismic tomography. Geophysics 54:200–215

Catalano S, Romagnoli G, Torrisi S, Tortorici G (2004) Evoluzione neogenico-quaternaria dei Monti Iblei: aspetti geologici, morfologici e tettonici. Atti del 2° Seminario Internazionale di Studi sul Carsismo negli Iblei e nell'Area sud Mediterranea, Speleologia Iblea12:39-52, Ragusa

CEN (2004) Eurocode 8—design of structures for earthquake resistance. Part 1: general rules, seismic actions and rules for buildings. European standard EN 1998-1, December 2004, European Committee for Standardization, Brussels

Cosma C, Heikkinen P, Keskinen J, Enescu N (2001) VSP in crystalline rocks from down-hole velocity profiling to 3D fracture mapping. Int J Rock Mech Min Sci 38:843–850

Cultrera G, Rovelli A, Mele G, Azzara R, Caserta A, Marra F (2003) Azimuth-dependent amplification of weak and strong ground motions within a fault zone (Nocera Umbra, central Italy). J Geophys Res 108(B3):101–1014. doi:10.1029/2002JB001929

Gardner GHF, Gardner LW, Gregory AR (1974) Formation velocity and density—the diagnostic basics for stratigraphic traps. Geophysics 39:770–780

Grasso M, Reuther CD, Tortorici L (1992) Neotectonic deformations in SE Sicily: the Ispica fault, evidence of Late Miocene-Pleistocene decoupled wrenching within the central Mediterranean stress regime. J Geodyn 16(1/2):135–146

Hunter JA, Benjumea B, Harris JB, Miller RD, Pullan SE, Burns RA, Good RL (2002) Surface and downhole shear wave seismic methods for thick soil site investigations. Soil Dyn Earthq Eng 22(9–12):931–941

Imposa S, Corrao M, Barone F, Coco G, Occhipinti R, Mozzicato P (2010) Geostructural and geognostic survey for a stability analysis of the calcareous cliff of Ispica (Hyblean plateau, south-eastern Sicily). Bull Eng Geol Environ 69(2):247–256

Kanli AI, Tildy P, Prónay Z, Pinar A, Hermann L (2006) *Vs*30 mapping and soil classification for seismic site effect evaluation in Dinar region, SW Turkey. Geophys J Int 165:223–235. doi:10.1111/j.1365-246X.2006.02882.x

Lai CG, Foti S, Godio A, Rix GJ, Sambuelli L, Socco LV (2000) Caratterizzazione geotecnica dei terreni mediante l'uso di tecniche geofisiche. Rivista Italiana di Geotecnica 34(3): 99–118 (ISSN: 0557–1405)

Lentini F (1986) Carta geologica del settore nord-orientale ibleo, scala 1:50.000. Università di Catania, Istituto di Scienze della Terra, S.EL.CA, Firenze

Liu E, Crampin S, Queen JH (1991) Fracture detection using crosshole surveys and reverse vertical seismic profiles at the Conoco borehole test facility, Oklahoma. Geophys J Int 107:449–463

Louis IF, Makropoulos CC (2001) Geophysical investigations at Akrotiri Archaeological site on Thera Island. Technical Report, Archaeological Society at Athens, Athens

McMechan GA (1983) Seismic tomography in boreholes. Geophys J Royal Astr Soc 74:601–605

Park CS, Lim JY, Choi CL, Kong Bc, Mok YJ (2008) Recent development of borehole seismic tests. The 14th world conference on earthquake engineering, October 12–17, 2008, Beijing, China

Philips WS, Fehler MC (1991) Travel time tomography: a comparison of popular methods. Geophysics 56:1642–1643

Price DG (2009) In: de Freitas MH (ed) Engineering geology: principles and practice, XVIII edn. Springer, Berlin, p 450

Pullammanappallil SK, Louie JN (1994) A generalized simulated-annealing optimization for inversion of first-arrival times. Bull Seismol Soc Am 84(5):1397–1409

Pullan SE, MacAulay HA (1987) An in-hole shotgun source for engineering seismic surveys. Geophysics 52:985–996

Quijada MF, Stewart RR (2007) Density estimations using density–velocity relations and seismic inversion. CREWES Res Rep 19:1–20

Roser J, Gosar A (2010) Determination of *Vs*30 for seismic ground classification in the Ljubljana area, Slovenia. Acta Geothecnica Slovenica 1:61–76

Taillandier C, Noble M, Chauris H, Calandra H (2009) First-arrival traveltime tomography based on the adjoint-state method. Geophysics 74(6):57–66